J. Fluid Mech. (2005), *vol.* 532, *pp.* 345–364.
doi:10.1017/S0022112005004143 Printed in the United Kingdom

Turbulence development in a non-equilibrium turbulent boundary layer with mild adverse pressure gradient

By C. D. AUBERTINE[1] AND J. K. EATON[1]

[1]Department of Mechanical Engineering, Stanford University, Stanford, CA, USA

(Received 24 July 2003 and in revised form 20 January 2005)

High-resolution laser-Doppler anemometer measurements were acquired in a two-dimensional turbulent boundary layer over a 4° ramp. The goals were to provide a detailed data set for an adverse pressure gradient boundary layer far from separation and to examine near-wall behaviour of the Reynolds stresses as compared to flat-plate boundary layers. The flow develops over a flat plate, reaching a momentum thickness Reynolds number of 3350 at an upstream reference location. The boundary layer is then subjected to a varying pressure gradient along the length of the ramp and partially redevelops on a downstream flat plate. Mean velocity measurements show a log law region in all velocity profiles, but the outer layer does not collapse in deficit coordinates indicating that the boundary layer is not in equilibrium. Measurements of non-dimensional stress ratios and quadrant analysis of the two-component data indicate relatively small changes to the turbulence structure. However, the streamwise normal stress has an extended outer layer plateau, and the shear stress and wall-normal stress have outer layer peaks. Near the wall, the streamwise normal stress and shear stress collapse with flat-plate data using standard scaling, but the wall normal stress is substantially larger than flat-plate cases.

1. Introduction

Adverse pressure gradient boundary layers occur in many technologically important geometries including diffusers and the trailing edges of airfoils. Most of the previous work involving adverse pressure gradients has involved flows at or near separation, equilibrium turbulent boundary layers, as originally proposed by Clauser (1954), or flows in complex geometries. Samuel & Joubert (1974) examined an increasingly adverse pressure gradient and noted that other than the law of the wall, none of the existing models works for predicting or collapsing the data. Spalart & Watmuff (1993) compared direct numerical simulation (DNS) and experimental work at low Reynolds numbers, and found that the DNS produced results which matched the experimental data, but they noted a lack of universality in their results. Tsuji & Morikawa (1976) examined a flow with alternating sign pressure gradients and found that the flow was in equilibrium for the initial adverse pressure gradient; however, as the sign of the pressure gradient alternated, the flow departed from equilibrium and did not return to an equilibrium state. Tulapurkara, Khoshnevis & Narasimhan (2001) studied an adverse pressure gradient boundary layer in a straight diffuser and noted that the turbulent kinetic energy and shear stress increase over the values for a flat plate.

Many groups have examined flows with incipient separation, near separation or just after separation. Dengel & Fernholz (1990) created an axisymmetric boundary layer

with incipient separation and examined mean velocity and stress profiles for three values of the skin friction, all near zero. They found that the mean velocity profile shape is not universal since the presence of the pressure gradient causes it to change constantly. They also found that the turbulence stress levels increase throughout the flow and do not become universal or asymptotic. Alving & Fernholz (1996) examined a flow with mild separation and downstream reattachment and noted that the mean shear decreases near the wall, while increasing as it moves away from the wall. They also observed that the production and Reynolds stress peaks move to roughly the middle of the boundary layer, and the normal stress terms increase in importance as separation is approached.

Skote & Henningson (2002) performed DNS on strong adverse pressure gradient flows with and without separation and found that there are two limits, zero pressure gradient and separation, and that between these limits, Reynolds-number effects occur in the velocity profiles. They also noted that far from the wall, the mean velocity profiles could be collapsed using a common pressure gradient velocity scale of $u_p = ((\nu/\rho)(\mathrm{d}P/\mathrm{d}x))^{1/3}$.

Clauser (1954) defined an equilibrium boundary layer as one subjected to a constant force history, leading to a well-defined upstream history of the flow. Since the downstream development of a boundary layer depends on the upstream history of the flow as well as on the local conditions, Clauser's goal was to develop a flow which had a constant history and thus a well-defined past. He defined a pressure gradient parameter β:

$$\beta = \frac{\delta^*}{\tau_o}\frac{\mathrm{d}P}{\mathrm{d}x}, \tag{1.1}$$

where the pressure gradient is scaled by the wall shear stress, τ_o, and the displacement thickness, δ^*. When β is maintained at a constant value, the boundary layer is in equilibrium. This requires a changing pressure gradient since the displacement thickness and wall shear change as the flow develops in the pressure gradient.

Following Clauser, many groups have examined variations on these equilibrium boundary layers. Bradshaw (1967) examined turbulent boundary layers for a wide range of values of β and found that as β increased, the value of the maximum shear stress also increased. Mellor & Gibson (1966) examined the effect of the pressure gradient on the outer flow, defining a pressure velocity $u_p = \sqrt{(\delta^*/\rho)(\mathrm{d}P/\mathrm{d}x)}$ which they then used to define a new mean velocity defect law. Cutler & Johnston (1989) studied the relaxation toward equilibrium of a boundary layer after reattachment in an adverse pressure gradient boundary layer. They noted that following reattachment, the eddy viscosity peak rises above the value at reattachment and only very far downstream as the flow approaches equilibrium does the eddy viscosity approach a self-similar profile. They also found that the mixing length near the centre of the layer rises rapidly to a peak value and then falls slowly to a value above the standard outer-layer value. The mixing length model was shown not to be a good model for these flows. Skåre & Krogstad (1994) found that equilibrium boundary-layer mean profiles collapse well in both inner and outer coordinates at fixed β. They noted that β has no effect on the von Kármán constant in the logarithmic law of the wall. They also observed that the turbulent stress profiles do not collapse as well in either inner or outer coordinates. Krogstad & Skåre (1995) examined an equilibrium boundary layer subjected to a strong adverse pressure gradient and found that the turbulent kinetic energy develops a second peak about halfway through the boundary layer, which affects the dissipation and diffusion rates in the outer layer. They also noted

that strong anisotropy was dominant only close to the wall based on their quadrant analysis work. Krogstad & Kaspersen (2002) also examined the turbulent kinetic energy and the peaks in the production term. They noted that the outer peak moved towards the centre of the boundary layer with increasing pressure gradient.

Some groups have proposed new scalings to collapse adverse pressure gradient data for a variety of different flows. Elsberry *et al.* (2000) studied an equilibrium boundary layer on the verge of separation and found that the flow was highly anisotropic. They noted that the turbulence was not in equilibrium with the mean flow and, when scaled on the free-stream velocity, the stresses were seen to increase with downstream distance. They also noted that the Reynolds stress correlation has a different value from that in flat-plate flows and does not remain constant as the downstream distance increases. They found it was possible to collapse the correlation using a new scaling $(\overline{u'v'}/\sqrt{\overline{u'^2v'^2}})(U_e/U_o)$. The value for U_0 is the maximum value of the free-stream velocity in the entire flow. The scaled correlation collapsed when plotted against a new length scale, $y/\theta Re_\theta^{0.2}$. The turbulent stresses were shown to collapse with the same length scale when scaled on U_0^2 for the streamwise and wall normal stresses and U_0U_e for the Reynolds shear stress. Bernard *et al.* (2003) examined half an airfoil and observed that the law of the wall was faithfully followed. They determined a length scale that allows the linear inner wake to tend toward a universal profile.

In addition to the experimental work, some analytical work has been done on adverse pressure gradient boundary layers to determine the appropriate length and velocity scales to collapse the profiles. Castillo & George (2001) did a similarity analysis on pressure gradient flows and found a parameter Λ:

$$\Lambda = \frac{\delta_{99}}{\rho U_\infty^2 \mathrm{d}\delta_{99}/\mathrm{d}x}\frac{\mathrm{d}P}{\mathrm{d}x}, \tag{1.2}$$

which takes on only three different values for all the boundary layers they examined. The parameter Λ has a different fixed value for each case of zero, adverse or favourable pressure gradient. This leads to three deficit profiles when plotted using the Zagarola & Smits (1998) scaling. Perry, Marusic & Jones (2002) developed a closure scheme for adverse pressure gradient boundary layers. Using this scheme, they found that once the mean flow evolution is correctly captured, the turbulence quantities could be determined using the work of Perry & Marusic (1995). Perry & Schofield (1973) developed a velocity defect law for adverse pressure gradient boundary layers based on the Reynolds stress profile.

The DeGraaff & Eaton (2000) mixed scaling has been observed to collapse the Reynolds stress profiles over a wide range of Reynolds numbers in the flat-plate boundary layer. The wall normal stress and the Reynolds shear stress use the standard normalization $\overline{v'^2}/U_\tau^2$, $\overline{u'v'}/U_\tau^2$, while the streamwise normal stress collapses when normalized as $\overline{u'^2}/U_\tau U_e$. Analytical work by Marusic & Kunkel (2003) has helped to explain the reason for this scaling. However, for more complex flows, such as those subject to pressure gradients, no scaling has been found that collapses all the turbulence stress data onto simple profiles.

DeGraaff & Eaton (1999) and Song & Eaton (2004) investigated complex boundary layers subjected to strong pressure gradients, separation and reattachment. They allowed the perturbed boundary layer to relax back towards equilibrium on a flat plate in each of these experiments and found that a stress equilibrium layer began to form adjacent to the wall as soon as the pressure gradient dropped to zero. Within the growing stress equilibrium layer, the normalized stress profiles were identical to

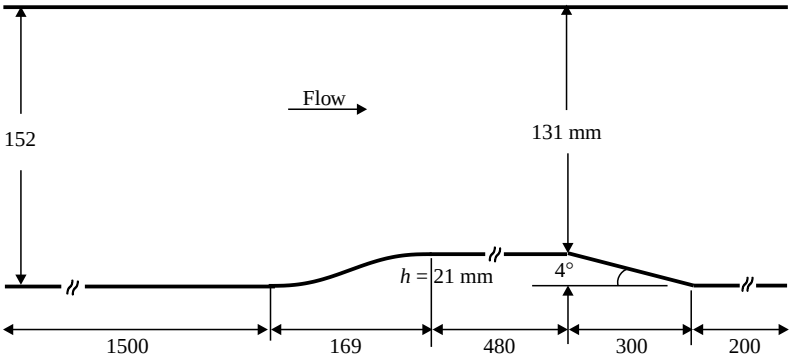

FIGURE 1. Current flow geometry.

the flat-plate profiles. For computational modelling, this result is useful because wall functions can be used confidently. However, it is only applicable in zero pressure gradient flows. A similar near-wall scaling valid in non-equilibrium pressure gradient flows would be very useful.

The objective of the current experiments is to examine a relatively mild adverse pressure gradient produced by a slow linear expansion of the test section. The pressure gradient should be large enough to perturb the boundary layer from its flat-plate state, but small enough to avoid separation. Stress measurements along the length of this extended region of pressure gradient can help to identify the existence of a universal scaling for such boundary layers. This paper describes the flow development and structural changes caused by the adverse pressure gradient, as well as examining previously proposed scalings to collapse the mean velocity and turbulence profiles.

2. Experiments

The experiments were performed in a closed-loop wind tunnel, which is mounted inside a pressure vessel. The measurements were made with a two-component high-resolution laser-Doppler anemometer (LDA) described by DeGraaff & Eaton (2001). The wind-tunnel test section has a rectangular cross-section of 152 mm $\times$ 711 mm and is 2.9 m in length. The boundary layer is tripped 150 mm downstream of a 5:1 contraction and develops over a 1.5 m long flat plate. The flow is then mildly contracted over a streamwise distance of 169 mm on the bottom wall, reducing the test-section height from 152 mm to 131 mm. The boundary layer then relaxes to equilibrium characteristics on a 480 mm long flat plate. At a typical free-stream velocity of 15 m s^{-1}, the free-stream turbulence level is approximately 0.2 %.

The current flow geometry (figure 1) consists of part of the 480 mm flat plate and a 4° linear expansion. The ramp expands the tunnel height from 131 mm to 152 mm. The flow does not separate along this ramp. The trailing edge of the ramp produced a small step in height between the ramp surface and the bottom surface of the wind tunnel. This step was patched using spackling and was sanded smooth. Owing to this non-ideal flow surface at the trailing edge of the ramp, the flow is perturbed by surface curvature, which is not well defined. The data gathered at this location are not included in the plots of turbulence measurements that follow, owing to this non-ideal surface.

The custom LDA has a measurement volume 35 μm in diameter and 60 μm in length. Owing to its small measurement volume, two of the major uncertainty

sources – velocity gradient bias and two-component coincidence are eliminated. The details, including the LDA bias correction, are found in DeGraaff & Eaton (2001). For 5000 samples, the uncertainties for U, $\overline{u'u'}$, $\overline{v'v'}$, $\overline{u'v'}$ are estimated as $\pm 1.5\,\%$, $\pm 4\,\%$, $\pm 8\,\%$ and $\pm 10\,\%$ of their local value in the centre of the profiles. The average data rate is approximately 25 Hz in the free-stream and considerably lower near the wall. Since the local values approach zero in the free-stream and near the wall, the relative uncertainties in those regions are larger. These uncertainties are estimates based on the statistical uncertainty of 5000 samples and the uncertainties associated with LDA fringe spacing, data filtering and velocity bias correction. The sample size was selected to minimize statistical uncertainty while avoiding possible problems due to very long sampling times.

All data reported here were acquired at a nominal free-stream velocity of $20.5\,\mathrm{m\,s^{-1}}$ and 1 atm of ambient pressure. The data were all gathered along the centreline of the wind tunnel in a fixed coordinate system with the x-direction along the tunnel and the y-direction normal to the flat-plate wall. The mean and turbulent stress data taken over the ramp were then rotated by 4° degrees to make them perpendicular to the wall for the purposes of analysis and scaling. The values for y used in all plots are in the rotated frame and can be taken as perpendicular to the bottom surface of the flow field at all locations.

The x-axis locations, x', are the physical locations normalized by the length of the 4° ramp. This non-dimensionalization is used for all locations with the location $x' = 0$ being located at the leading edge of the ramp and $x' = 1.00$ representing the trailing edge of the ramp. The upstream flat-plate location is therefore located at $x' = -0.33$ in this non-dimensionalization. The reference location is a flat-plate boundary layer, where the mean and turbulence profiles gathered were compared with prior flat-plate data to ensure that the reference location produced typical flat-plate behaviour.

Wall static pressure data were measured through 0.64 mm diameter surface pressure taps located along the ramp and along the flat plate over which the flow redevelops, using a differential pressure transducer (Setra model 264). This pressure distribution gives a varying value of β, the Clauser pressure gradient parameter, ranging from 0 on the flat plate, to -1 in the mild favourable pressure gradient before the start of the ramp and to a maximum value of 2.5 along the ramp. The value of β does not remain constant along the length of the ramp, but at all locations it is relatively small, indicating that this is a mild adverse pressure gradient. The maximum value of β observed in this flow is similar to the values from the mild adverse pressure gradient equilibrium boundary layer of Clauser, where the maximum value of β is about 2.3 (Coles & Hirst 1969). Skåre & Krogstad (1994) found values of β greater than 20 for a flow near separation.

Skin-friction measurements were made using the oil-fringe imaging method described by Monson, Mateer & Menter (1993) for all locations except for the two upstream flat-plate regions ($x' = -0.33$ and 0) at which a log-law fit was applied instead. This technique is non-intrusive and relates the wall shear to the thinning rate of a line of oil placed on the surface. The oil is placed on the surface at several locations and the tunnel is started impulsively. Most of the oil flows downstream during a short transient. The remaining oil forms a thin wedge which, when illuminated using monochromatic light, produces interference fringes with a uniform spacing near the leading edge of the oil film. The surface of the wind tunnel from 1 m upstream of the mild contraction until the end of the test section was covered with 0.13 mm thick green acetate with the back painted flat black to give better imaging quality. The green acetate was taped to the surface using double-sided tape and smoothed to

eliminate air pockets. For these experiments, Dow Corning 200 fluid with a viscosity of $5 \times 10^{-5}\,\mathrm{m^2\,s^{-1}}$ was applied in a 50 mm oil line using a sharp knife edge at the measurement location and at the upstream reference location. The oil line was oriented perpendicular to the flow and the wind tunnel was then run for approximately 10 min. When a fringe pattern was evident the tunnel was stopped and images were taken at the upstream reference location and the current measurement position. The images were gathered using a Kodak high-resolution digital camera (model DC290), and a green monochromatic diffuse light source, made of a white fluorescent light, green acetate and semi-transparent Mylar. Five independent measurements at each location were performed and the fringe spacing was averaged. The fringe spacing of the images was found to repeat within $\pm 2\,\%$.

The fringe spacing depends on the skin friction, but also on the time history of the flow, the properties of the oil, the surface properties and the viewing angle. Because of these limitations, it is very difficult to estimate the absolute value of the skin friction and, instead, the ratio of the skin friction at the location of interest to the reference location is used. The time history, oil and surface properties are the same at both locations. For the measurement locations after the trailing edge of the ramp, where both the measurement and reference surface are horizontal, the relationship between the skin friction, C_f, and fringe spacing, ΔS_f, can be simplified to:

$$\frac{C_{f,local}}{C_{f,ref}} = \frac{\Delta S_{f,local\ image}}{\Delta S_{f,ref\ image}}, \tag{2.1}$$

because the viewing angle for both the measurement and reference locations are the same. For the locations along the ramp, the viewing angle for the measurement and reference locations are different and the relationship between the skin friction and fringe spacing can be expressed as:

$$\frac{C_{f,local}}{C_{f,ref}} = \frac{\Delta S_{f,local\ image}}{\Delta S_{f,ref\ image}} \frac{\dfrac{\cos(a \sin(\sin\theta_{light,\,loc}/n_{oil}))}{\cos\theta_{camera,\,loc}}}{\dfrac{\cos(a \sin(\sin\theta_{light,\,ref}/n_{oil}))}{\cos\theta_{camera,\,ref}}}, \tag{2.2}$$

where n_{oil} is 1.4022 and the angles can be computed based on the 4° angle of the ramp.

3. Results and discussion

Figure 2 shows the static pressure distribution, normalized by the dynamic pressure at the upstream flat-plate location, $C_p = (P_{local} - P_{ref})/(0.5U_{ref}^2)$, plotted against the normalized distance along the test section. The flow initially developed over a flat plate and then was subjected to a mild adverse pressure gradient before redeveloping along another flat plate. The pressure distribution shows that the flow encounters a short region of mild favourable pressure gradient at the top of the ramp before passing into the moderate adverse pressure gradient. At the end of the ramp, the flow starts to recover towards a zero pressure gradient, however, it is still experiencing a very small favourable pressure gradient at the last measurement location.

The development of the skin-friction coefficient, C_f, is seen in figure 3, again plotted against the normalized distance along the test section. The skin-friction coefficient can be seen to increase in the mild favourable pressure gradient before decreasing along the ramp owing to the adverse pressure gradient. The boundary layer does not approach separation, but the skin friction still falls by a factor of nearly two

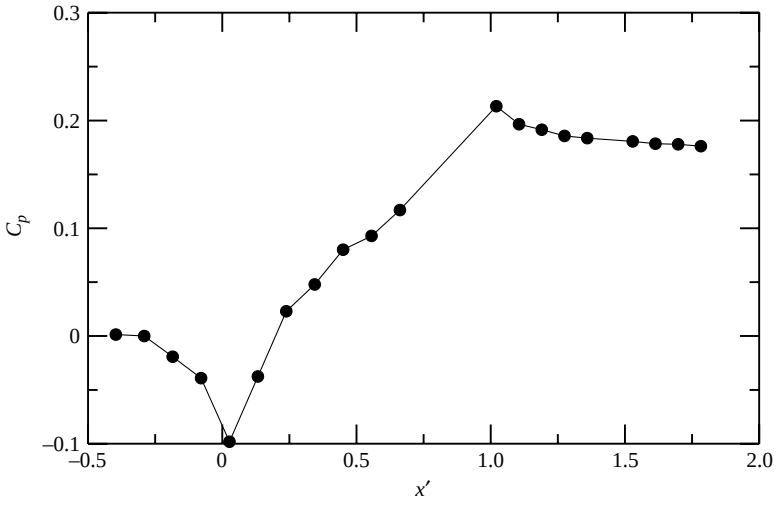

FIGURE 2. Bottom wall pressure distribution.

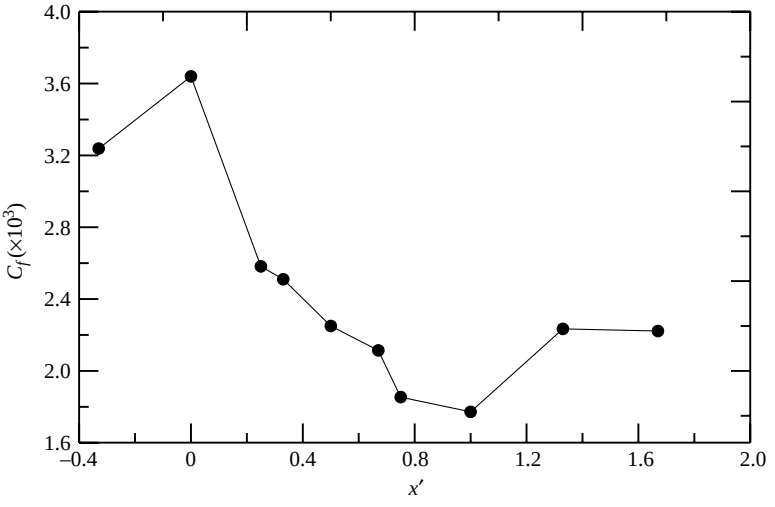

FIGURE 3. Skin friction distribution.

relative to the upstream boundary layer. The free-stream velocity decreases by only 11 % in the same distance. Once the flow starts redeveloping along the flat plate, the skin-friction coefficient again rises owing to the mild favourable pressure gradient before flattening out at the last measurement location.

Table 1 shows the development of the free-stream velocity, the boundary-layer thickness, the momentum thickness, the shape factor, the wake strength parameter and the momentum thickness Reynolds number, Clauser's pressure gradient parameter, β, and the pressure gradient velocity scale, u_p, used by Skote & Henningson (2002), along the length of the test section. This table also includes the symbols that are used in the following figures to represent each profile location, with open symbols used for data along the adverse pressure gradient ramp and closed symbols for the other locations. The shape factor initially decreases in the region of the flow subjected to the very mild favourable pressure gradient. Once the flow reaches the ramp, the

x'	U_e(m s^{-1})	δ_{99}(mm)	θ (mm)	H	Π	Re_θ	β	u_p(m s^{-1})	Symbol
−0.33	20.48	25.22	2.51	1.34	0.31	3330	−0.17	−0.04	●
0	20.62	23.81	2.17	1.29	−0.04	2990	−0.07	0.02	■
0.25	19.87	29.18	3.10	1.39	0.72	3990	2.07	0.11	□
0.33	19.60	30.41	3.32	1.39	0.72	4210	1.74	0.10	◇
0.5	19.20	33.77	3.78	1.42	0.87	4700	1.60	0.09	△
0.67	18.80	35.64	4.24	1.46	0.92	5160	2.31	0.09	▽
0.75	18.71	37.53	4.60	1.48	1.29	5570	1.38	0.05	○
1.00	18.23	41.76	5.66	1.56	1.24	6680	−1.41	−0.07	◆
1.33	18.26	39.78	5.37	1.47	0.54	6340	−0.37	−0.05	▲
1.67	17.54	38.77	5.26	1.45	0.67	6320	−0.18	−0.04	▼

TABLE 1. Flow parameters.

shape factor increases in a mostly linear way; however, the shape factor at the start of the ramp does not exhibit this linear trend and is the same for the first two locations. The wake strength parameter, also called Cole's wake parameter, can be seen to increase along the ramp. This parameter is a function of the Clauser pressure gradient parameter and is constant in equilibrium flows, again showing that this flow is not an equilibrium flow.

The development of the mean streamwise velocity profile is shown in figures 4 and 5. In figure 4, the velocity is normalized by the local free-stream velocity and the height above the wall is scaled using the height of the ramp. The fixed scaling for the y-coordinate has been chosen to show the boundary-layer growth. Figure 4(a) shows the mean velocity profiles for measurement locations on the ramp, which illustrate the relatively rapid boundary-layer growth. This boundary-layer growth is also evident in table 1, which shows that δ_{99} increases by 75 % along the length of the ramp. The shape factor behaviour, as discussed above, can also be noted in the mean velocity profiles shown here; each successive profile along the ramp becomes less full, corresponding to the monotonic increase in shape factor. No inflection point is observed in the profiles on the ramp, although one is usually expected in adverse pressure gradient flows. The lack of an inflection point is due to the weak nature of the adverse pressure gradient. For a laminar flow, the curvature of the velocity in the outer layer is negative and the curvature at the wall is positive owing to the adverse pressure gradient, so there must always be an inflection point. For a turbulent flow to have an inflection point in the mean velocity profile requires:

$$\left.\frac{\partial^2 U}{\partial y^2}\right|_{y=0} = \frac{1}{\mu}\frac{\mathrm{d}P}{\mathrm{d}x} - \frac{1}{\nu}\frac{\partial}{\partial y}(\overline{-u'v'}) \geqslant 0. \tag{3.1}$$

For an inflection point in an adverse pressure gradient flow:

$$\frac{\partial}{\partial y}(\overline{-u'v'}) \leqslant \frac{1}{\rho}\frac{\mathrm{d}P}{\mathrm{d}x} \quad \text{where } \frac{\mathrm{d}P}{\mathrm{d}x} \geqslant 0. \tag{3.2}$$

For the current flow, the derivative of the shear stress is approximately 2 m s^{-2}, while the pressure gradient term is approximately 0.5 m s^{-2}, therefore no inflection point will be present in this flow. Figure 5(a) shows the same mean velocity profiles in the law of the wall coordinates. Here the friction velocity calculated from the skin friction measured using oil flow interferometry is used to normalize the profiles. The profiles exhibit a substantial log region that could be used to estimate the skin friction;

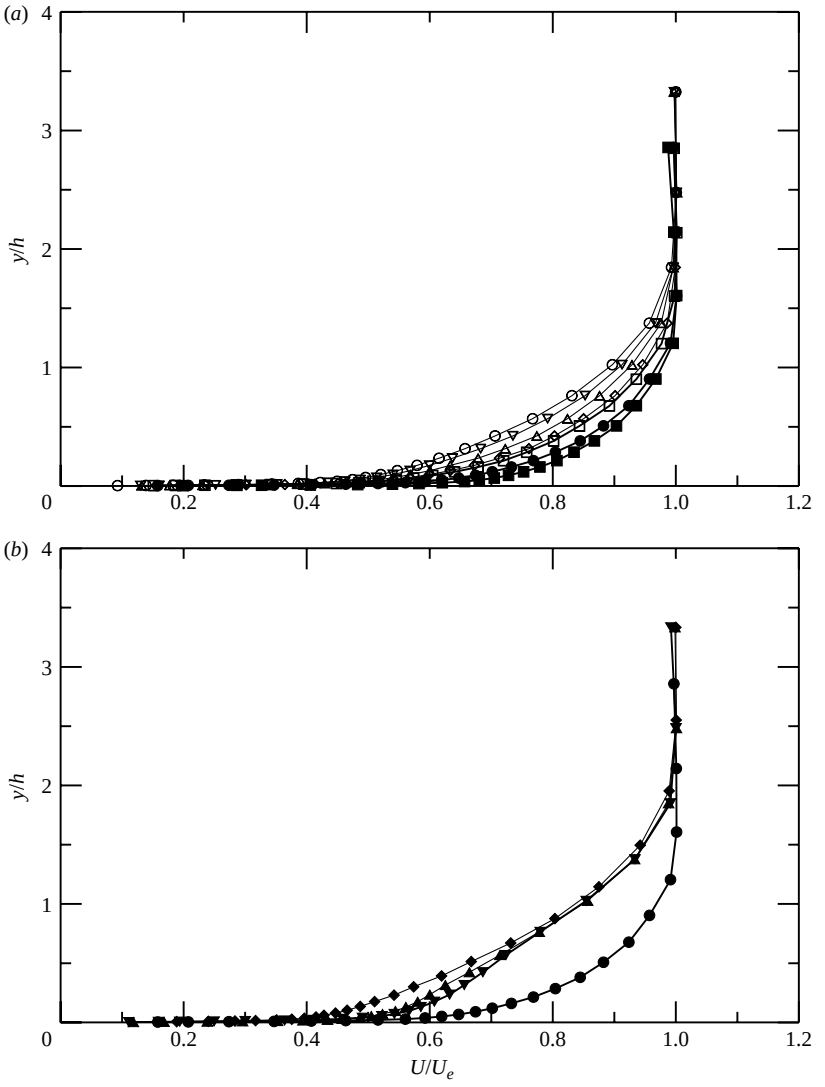

FIGURE 4. Mean flow development (*a*) flow along the ramp, (*b*) flow redevelopment.

however, as the flow moves downstream and the wake occupies an increasing fraction of the boundary-layer thickness, the outer part of the log region is cut off.

Figures 4(*b*) and 5(*b*) show the mean velocity profiles in the recovery region of the flow, beginning at $x' = 1.00$. The upstream boundary layer is shown for reference. These profiles have an obvious inflection point in the outer layer and look similar to boundary layers recovering downstream of a separation bubble. The boundary layers do not have the typical near-wall behaviour at $x' = 1.00$ and 1.33, although the logarithmic law of the wall is still followed. The profiles exhibit a very large wake profile, which decays as the flow travels downstream in the recovery region. These redevelopment profiles have highly non-equilibrium behaviour which can be observed in the turbulence, with the profiles exhibiting markedly different shapes from the relatively simple shapes obtained further upstream on the ramp. To avoid confusing the plots, the turbulence data for these two locations will not be shown below. Data

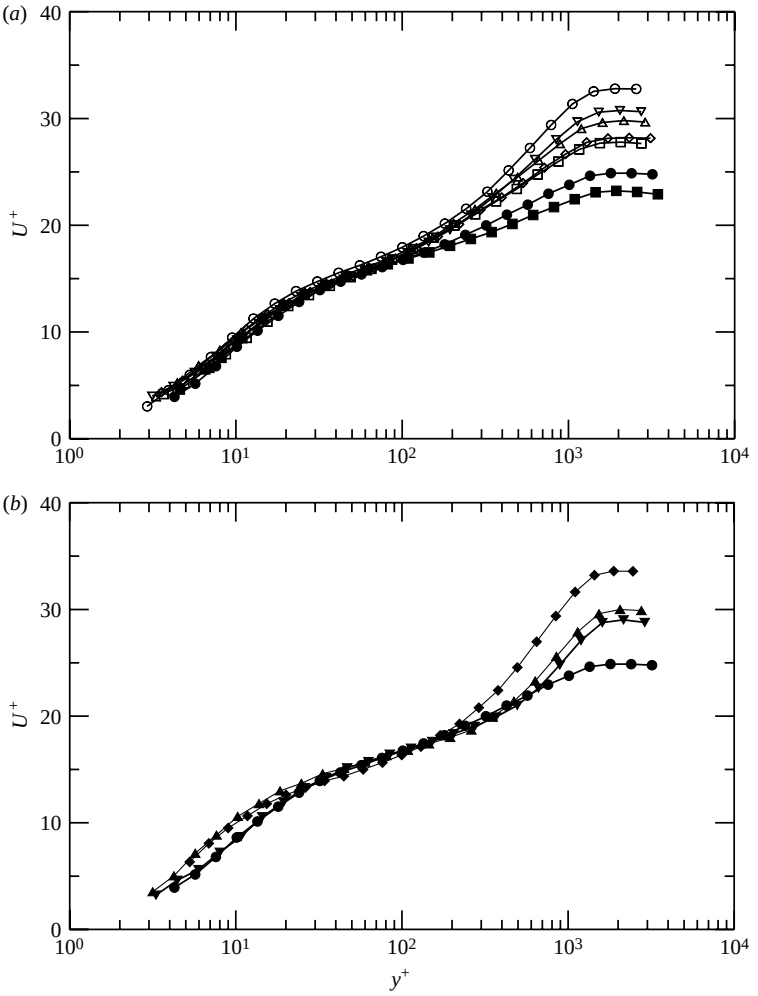

FIGURE 5. Mean flow development in the law of the wall coordinates (*a*) flow along the ramp, (*b*) flow redevelopment.

from the most downstream location will be shown to demonstrate the recovery of the boundary layer towards flat-plate behaviour.

The wall-normal component of the mean velocity was also measured, although, for brevity, it is not plotted here. It remains small throughout the flow field, indicating that the boundary layer remains far from separation.

Figure 6 shows the mean deficit profile plotted in the coordinates proposed by Zagarola & Smits (1998) for all the locations along the flow subjected to an adverse pressure gradient. The profiles do not appear to collapse very well, regardless of the pressure gradient at each location, in disagreement with the work of Castillo & George (2001). This lack of collapse can be expected owing to the changing mean velocity profile shape, similar to the changing profile shape observed by Dengel & Fernholz (1990). For this adverse pressure gradient, Λ has a value of 0.22 when evaluated using the method of Castillo & George (2001), which is the value given in their work for adverse pressure gradient flows.

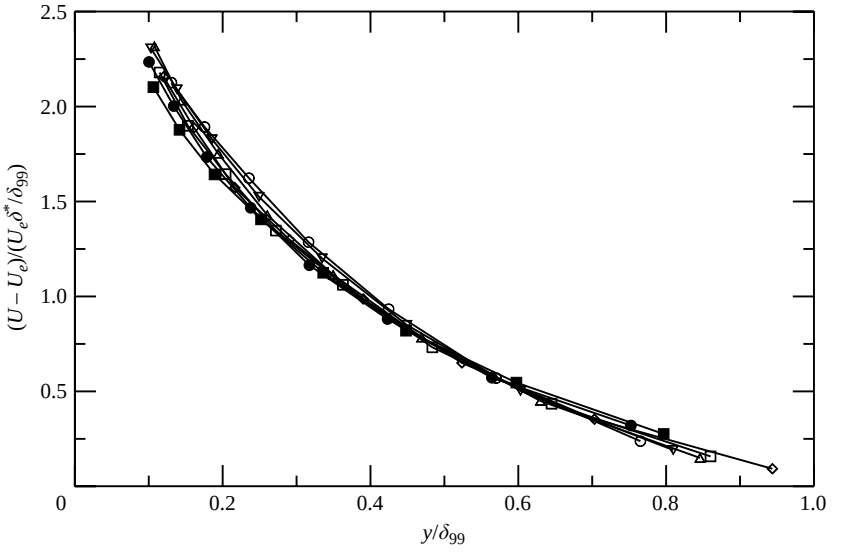

FIGURE 6. Mean flow deficit profile in adverse pressure gradient locations.

The development of the turbulent stresses is shown in figure 7, normalized using the mixed scaling proposed by DeGraaff & Eaton (2000). All the stresses are plotted with the height above the wall scaled in the rotated frame in inner coordinates. As the streamwise normal stress develops in the adverse pressure gradient, an extended plateau of elevated normal stress dominates the outer layer. This plateau increases in relative intensity when compared with the inner-layer plateau as the flow continues along the ramp. When the flow returns to a flat plate the plateau starts to decay, although it is still clearly present at the last measurement location. The inner peak collapses very well in the DeGraaff & Eaton mixed scaling, except for the mild favourable pressure gradient location where curvature effects may be important. The outer peak and outer region of the streamwise normal stress can be collapsed using the Elsberry *et al.* (2000) stress scaling and the boundary-layer thickness as the length scale as shown in figure 8. In this case, the value of $U_{e,max}$ is the free-stream value at the leading edge of the ramp, as this is the maximum free-stream velocity measured in this flow. Since $U_{e,max}$ is a constant, this is essentially a dimensional plot of the streamwise normal stress. The good collapse indicates that the outer-layer turbulence levels are unchanged by the adverse pressure gradient and the mean velocity profile changes it causes. This is clearly a non-equilibrium effect.

The wall normal stress scaled by U_τ^2 shows good collapse in the inner region for the adverse pressure gradient locations; however, the flat-plate locations, at $x' = -0.33$, 0 and 1.67, do not collapse along with the adverse pressure gradient data. Dimensionally, the peak value of the wall normal stress when unscaled remains constant along the flow and the location of the peak moves away from the wall so that it remains at the same relative height within the boundary layer. The Reynolds shear stress scaled in the flat-plate scaling shows good collapse for both the adverse pressure gradient data and the upstream flat-plate boundary-layer data. Only the downstream redevelopment data do not collapse in this scaling. The Reynolds shear stress also develops an outer peak which decays as the flow redevelops.

Other scalings for the turbulent stresses in adverse pressure gradients have been proposed previously. Some of these scalings were examined for the current flow, but

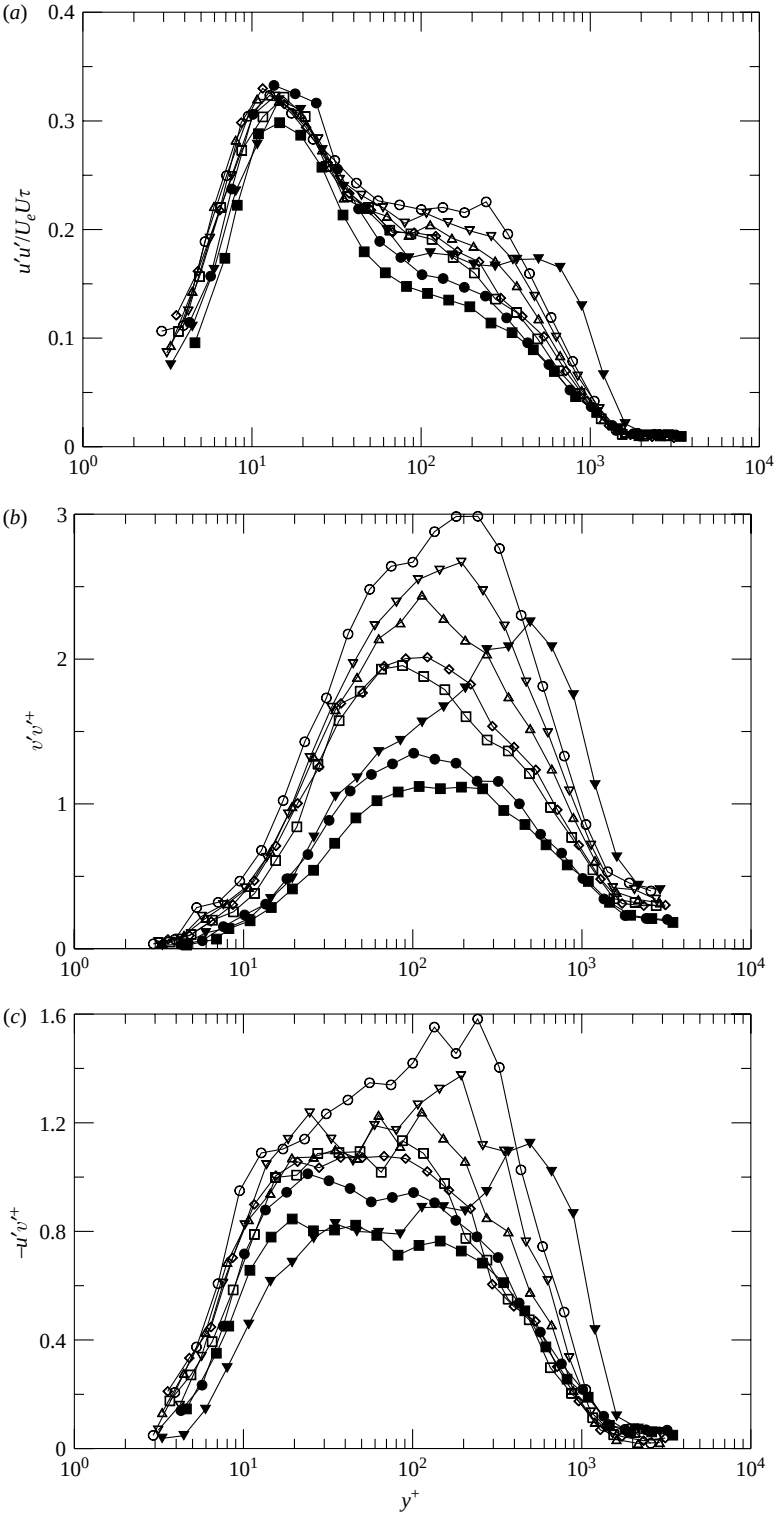

FIGURE 7. Stress development for the (*a*) streamwise normal, (*b*) wall normal and (*c*) Reynolds shear stress components.

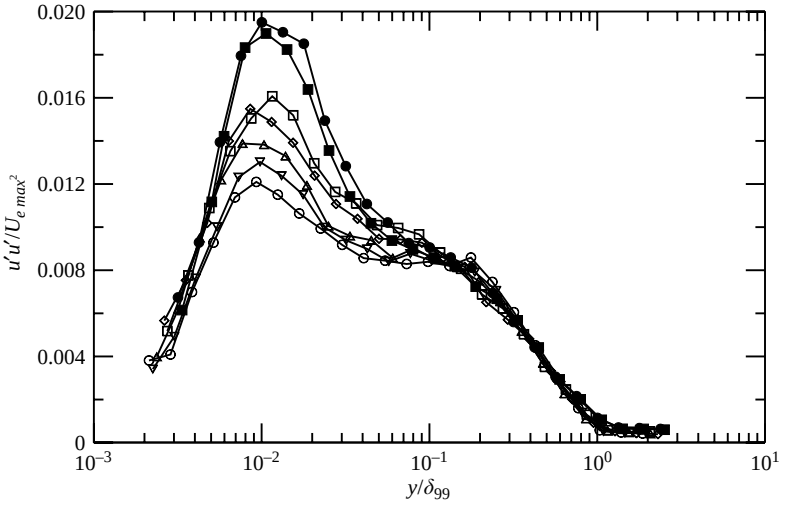

FIGURE 8. Streamwise normal stress collapse – outer layer.

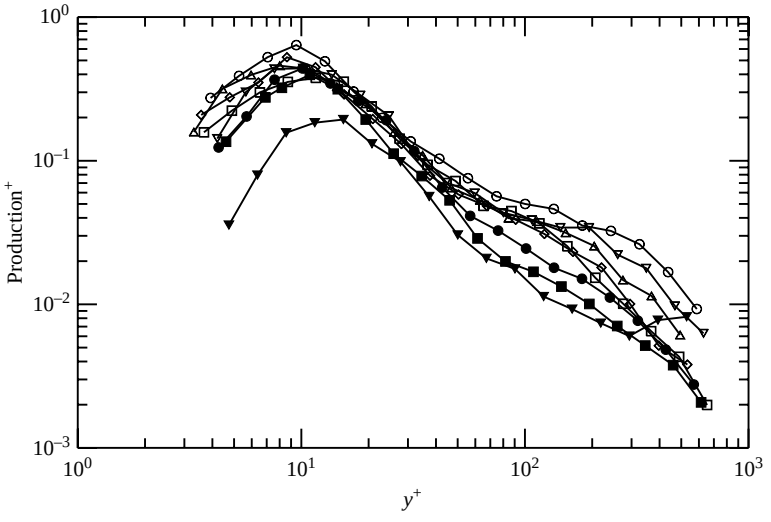

FIGURE 9. Production development.

many could not be applied to the current flow for a variety of reasons. The Perry & Schofield (1973) scaling could not be tested as its limit of applicability occurs when the maximum shear stress is at least 1.5 times larger than the wall shear. For the flow examined here this is only true for one of the data sets in the adverse pressure gradient region of the flow. Because the shape factor does not remain constant and the flow is not in equilibrium, the scaling proposed by Elsberry *et al.* (2000) does not collapse most of the stress data for this flow. The work of Bernard *et al.* (2003) is also not applicable because, for a flat ramp, as was used in this work, the new length scale is identical to the mixing-length parameter defined by Prandtl, as the curvature of a flat ramp causes the additional correction term to drop out for this geometry.

Figure 9 shows the development of the production of turbulent kinetic energy. The production term and the height above the wall are normalized in local inner variables.

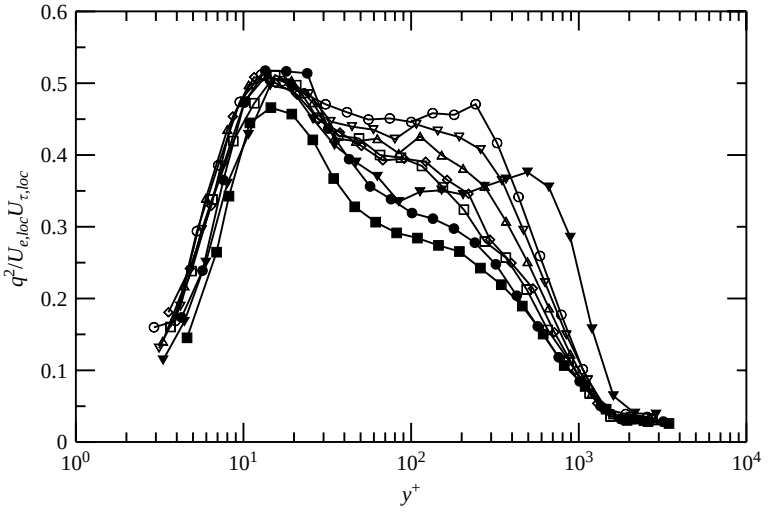

FIGURE 10. Turbulent kinetic energy development.

The peak value is observed to change very slightly in the adverse pressure gradient region, with a slight decrease observed at the start of the ramp, which quickly recovers to a value near that observed in the flat-plate boundary layer. The redevelopment location shows that the production is much lower once the pressure gradient is removed. The value of the slope of the production curve in the log region is -1 for the flat-plate case, showing that the flow is in local equilibrium. However, for the mild favourable and the adverse pressure gradient profiles the slope is distinctly different from -1, indicating that the turbulence is out of equilibrium even though there is still a logarithmic region in the mean profile. Unlike the work by Skåre & Krogstad (1994), where two peaks were observed in the production term, only one peak is observed in these data. The inner peak, which is observed here, is due to the increase of the mean strain as the wall is approached. The outer peak that was observed by Skåre & Krogstad (1994) is due to the peak in the turbulence stresses, which they noted was caused by the strong adverse pressure gradient in their experiment. In the current case, the outer peak in the Reynolds shear stress produces only a small bump in the outer-layer production, which decays away rapidly in the redevelopment region. The weaker pressure gradient in the current case results in a simpler turbulence structure.

Figure 10 shows the development of q^2, approximated using $q^2 = 3(\overline{u'^2} + \overline{v'^2})/2$ over the ramp. The mixed scaling collapses the inner peak well except for the profile at $x' = 0$. This is because q^2 is dominated by the $\overline{u'^2}$ term. In the outer layer, the value of q^2 increases rapidly at the start of the adverse pressure gradient and then increases more slowly as the flow proceeds along the adverse pressure gradient, forming an outer peak similar to those seen in the individual stresses. This peak starts to decay as the flow recovers, but is still present at the last measurement location.

The Townsend structure parameter, $a_1 = \overline{u'v'}/q^2$ is shown in figure 11. The values of the structure parameter were smoothed using a weighted average of the point and its nearest neighbours. The Townsend structure parameter for a flat-plate boundary layer is generally taken to be constant and have a value of 0.15 (Bradshaw 1967). Then, as the adverse pressure gradient is imposed, the Townsend structure parameter decreases in value to approximately 0.14 for all the locations in the adverse pressure gradient. The Townsend parameter is seen to decrease near the outer edge of the boundary

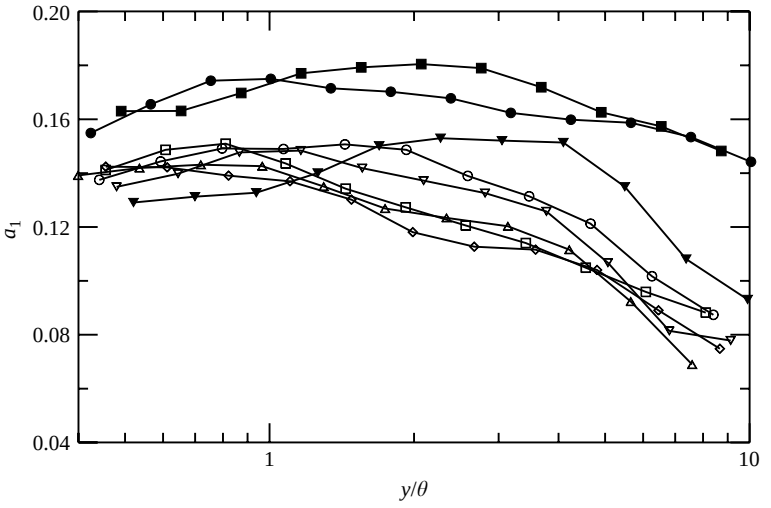

FIGURE 11. Townsend parameter development.

layer as noted by Bradshaw (1967). Bradshaw attributed this to the irrotational motions becoming comparable in intensity to the turbulence fluctuations. Spalart & Watmuff (1993) also noted this dip in the outer region of the boundary layer in their experimental and computational work. Skåre & Krogstad (1994) found that the structure parameter was constant, but slightly lower for the adverse pressure gradient case than for the zero pressure gradient case, which is seen in the inner region here. Their plot also shows the same dip in the outer region of the boundary layer as observed by Bradshaw and in the data shown here. As the flow redevelops, the Townsend parameter relaxes back towards its flat-plate value, particularly in the outer region where the value increases rapidly back to near the flat-plate value while the inner region increase is much slower. The slow recovery in the inner layer is similar to that observed by Alving & Fernholz (1996), where in their separated flow the outer layer recovered much more rapidly than the inner layer. Alving & Fernholz (1996) concluded that this was due to large-scale outer-layer structures, which survive the separation process and interfere with the inner region redevelopment. Although the flow does not separate, similar structures may be present in this flow causing similar effects in the redevelopment region.

The development of the anisotropy parameter, $\overline{v'v'}/\overline{u'u'}$, plotted against the height above the wall scaled on the boundary-layer thickness, is shown in figure 12. The anisotropy parameter for the flat-plate location varies between 0.3 and 0.4 throughout most of the boundary layer. As the adverse pressure gradient is imposed, the anisotropy parameter increases slightly, but monotonically. This indicates that the turbulence is becoming slightly more isotropic. After the pressure gradient is removed, the anisotropy parameter does not recover to the zero pressure gradient value over the development length examined. The relatively small changes in the anisotropy parameter indicate that the normal stress components respond almost equally to the imposed adverse pressure gradient. This implies that there is little effect owing to streamline curvature.

Figure 13 shows the Reynolds stress correlation plotted against the height above the wall scaled on the boundary-layer thickness. The flat-plate profile shows a mostly constant correlation with a value of approximately 0.40. As the flow encounters

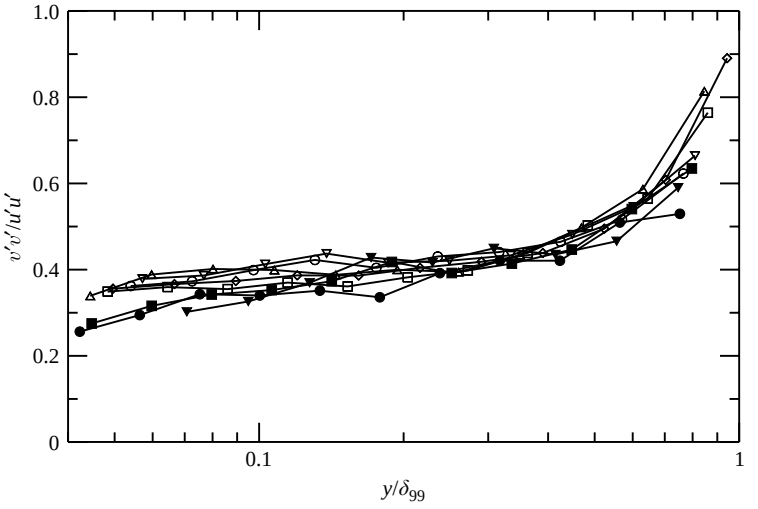

FIGURE 12. Anisotropy development.

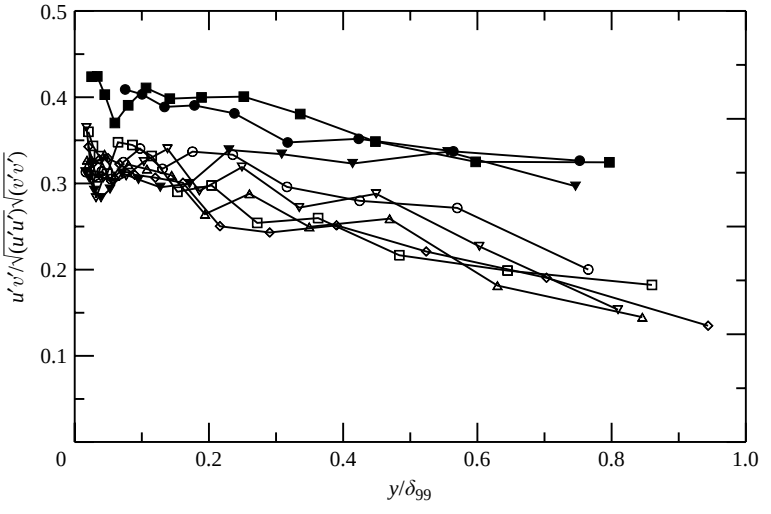

FIGURE 13. Reynolds stress correlation development.

the adverse pressure gradient the correlation coefficient decreases to a value of approximately 0.30 and remains at this value until the flow redevelops on the flat plate, at which point the coefficient starts to increase back to a value near that of the initial flat-plate profile. This effect due to the adverse pressure gradient is different from what was observed by Skåre & Krogstad (1994). They found that the value of the Reynolds stress correlation was approximately the same for their flow near separation as it was for the zero pressure gradient case. The difference here may be related to the differences in pressure gradient. The results shown here are also unlike those observed by Elsberry *et al.* (2000) who noted that the Reynolds stress correlation varied with streamwise position in an adverse pressure gradient flow. The difference in the observations in the current data and in their work may also be due to strength of the adverse pressure gradient.

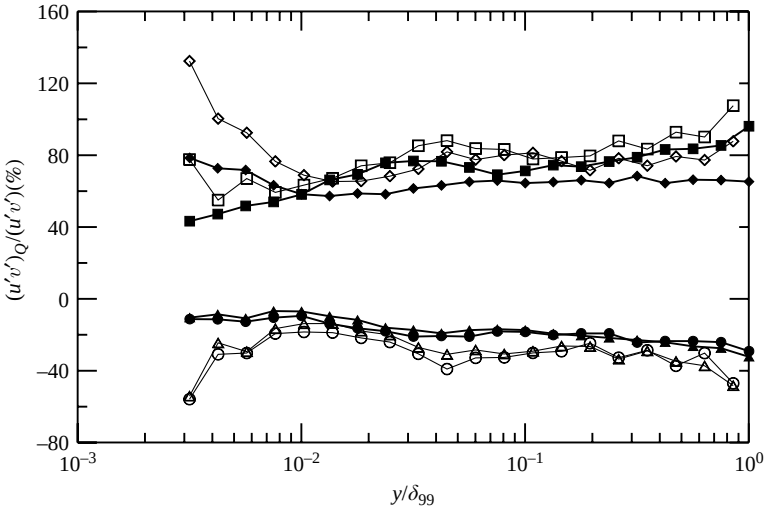

FIGURE 14. Quadrant analysis comparison $H = 0$ (closed symbols represent upstream reference location, open symbols represent the adverse pressure gradient location) (●, $Q1$; ■, $Q2$; ▲, $Q3$; ◆, $Q4$).

Quadrant analysis for examining the structure of turbulence and the relative contribution of sweeps and ejections was introduced by Wallace, Eckelmann & Brodkey (1972). Lu & Willmarth (1973) developed the concept of a hyperbolic hole of size H and then defined the contribution to the Reynolds shear stress of each quadrant (Q) as:

$$(u'v')_Q = \frac{1}{N}\sum u'v'I_Q, \tag{3.3}$$

where N is the number of samples acquired by the LDA and I_Q is an indicator function defined as:

$$I_Q = \begin{cases} 1 & \text{where } |u'v'|_Q \geqslant Hu''v'', \\ 0 & \text{otherwise.} \end{cases} \tag{3.4}$$

The double prime is used to indicate an r.m.s. value of a fluctuating velocity component.

Krogstad & Skåre (1995) performed quadrant decomposition on their equilibrium flow and found that when looking at all events, ($H = 0$), for both the adverse pressure gradient and the flat-plate boundary layer, sweep ($Q4$) events dominated the flow in the near-wall region, while outside this region in both boundary layers, the effects of ejections ($Q2$) and sweeps ($Q4$) were similar. For the flat-plate boundary layer, the combined contribution due to sweeps ($Q4$) and ejections ($Q2$) was smaller than the combined effect for the adverse pressure gradient boundary layer, implying an increase in the importance of outward and inward interactions ($Q1$, $Q3$), with the outward interactions ($Q1$) being more important. When only strong events ($H = 4$) were examined, the contributions of outward interactions ($Q1$) were observed to be much more important in the adverse pressure gradient boundary layer than in the flat plate.

Quadrant analysis performed on the current data showed that, for $H = 0$, the adverse pressure gradient increases the magnitude of the effects of all four components. The sweep and ejection ($Q4$, $Q2$) events are dominant for all locations in the flow over the outward and inward interaction ($Q1$, $Q3$) events. Figure 14 shows the four

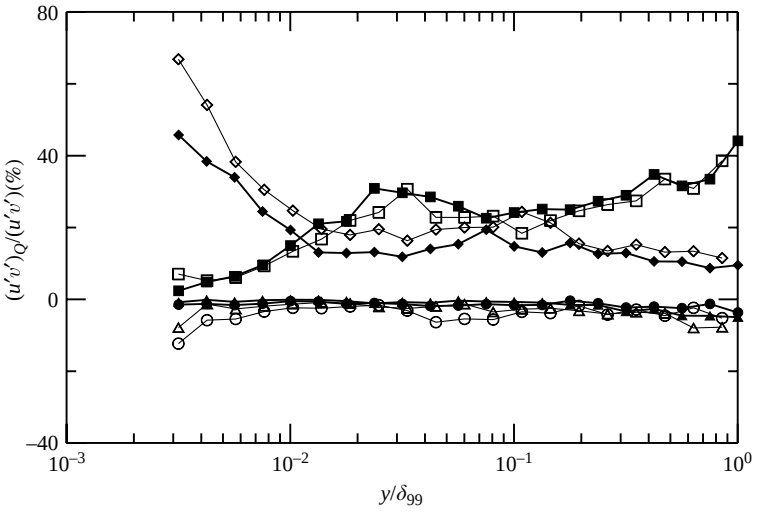

FIGURE 15. Quadrant analysis comparison $H = 2.5$ (closed symbols represent upstream reference location, open symbols represent the adverse pressure gradient location) (●, $Q1$; ■, $Q2$; ▲, $Q3$; ◆, $Q4$).

different quadrant results for both the flat-plate location and an adverse pressure gradient location, 2/3 of the way down the ramp. The quadrant decomposition, shown as a percentage, is plotted against the height above the wall scaled on the boundary-layer thickness. When examining all streamwise locations, the sweeps ($Q4$) and ejections ($Q2$) are very similar in contribution throughout the boundary layer with sweeps contributing slightly less in the outer portion of the boundary layer and contributing slightly more in the inner portion. Figure 15 shows a comparison of the four different quadrant decomposition results for moderate and strong events ($H = 2.5$), for both the flat-plate region of the flow and for the flow along the ramp. The results at other locations in the adverse pressure gradient look similar, and the results are also similar for $H = 4.0$, strong events. The sweep ($Q4$) events for the adverse pressure gradient contribute a slightly smaller percentage of the total when compared to the flat plate case for the middle of the boundary layer, while being significantly less than in the flat-plate case in the very near wall region. In addition, for moderate and strong events the ejection ($Q2$) events are suppressed near the wall and dominated by the sweep ($Q4$) events, while in the outer part of the boundary layer the ejection ($Q2$) events are dominant, as seen by Krogstad & Skåre (1995). However, when the sum of the contributions of ejection and sweep ($Q2$, $Q4$) events for the adverse pressure gradient is compared with the results for zero pressure gradient, the current data show no notable difference between the two cases.

4. Conclusions

Experimental measurements using a high-resolution LDA system have been presented for the flow along a 4° expansion ramp in which the Clauser parameter, β, is relatively small and varies slowly along the length of the ramp. The inner layer follows the standard logarithmic law of the wall, but the extent of the log region shrinks, in wall coordinates, going downstream as the wake occupies a larger fraction of the boundary-layer thickness. Although the pressure gradient is mild and

there is no inflection point in the mean velocity profile, the boundary layer is not in equilibrium. The shape of the mean velocity profile continues to evolve along the entire length of the flow, which leads to the mean velocity profile not collapsing in deficit coordinates as proposed by Castillo & George (2001).

Profiles of the three measured Reynolds stress components are similar in the inner layer to flat-plate profiles, but consistently show higher levels in the outer layer. The streamwise normal stress agrees closely with the flat-plate data near the wall when plotted using the DeGraaff & Eaton (2000) mixed scaling, computed from the local skin friction and free-stream velocity. However, there is a plateau of elevated normal stress in the log and wake regions of the flow. The scaling proposed by Elsberry *et al.* (2000), which in this case is equivalent to a fixed dimensional representation of the data, collapses the outer region of the streamwise normal stress. This means that the outer-layer streamwise velocity fluctuations do not change significantly even as the mean profile evolves, a classic non-equilibrium boundary layer. The other two stresses develop substantial peaks in the log layer that do not collapse with the flat-plate data. These peaks decay when the adverse pressure gradient is removed.

The mild adverse pressure gradient causes only small effects on the structure of the turbulence. Most non-dimensional structural parameters show only small changes as the flow enters the adverse pressure gradient region, although Townsend's structural parameter, $a1$, shows a consistent reduction. The recovery of this parameter downstream of the ramp is slower near the wall than in the outer layer in agreement with earlier results of Alving & Fernholz (1996). A quadrant analysis examining the relative importance of sweeps and ejections indicates a relatively small effect of the mean profile changes.

Overall, the detailed data set presented here offers a considerable challenge to modellers owing to the non-equilibrium effects which have a substantial impact on the mean velocity and Reynolds stress profiles.

We gratefully acknowledge the financial support from the Office of Naval Research contract N00014-00-10078.

REFERENCES

Alving, A. E. & Fernholz, H. H. 1996 Turbulence measurements around a mild separation bubble and downstream of reattachment. *J. Fluid Mech.* **322**, 297–328.

Bernard, A., Foucaut, J. M., Dupont, P. & Stanislas, M. 2003 Decelerating boundary layer: a new scaling and mixing length model. *AIAA* **41**, 248–255.

Bradshaw, P. 1967 The turbulence structure of equilibrium boundary layers. *J. Fluid Mech.* **29**, 625–645.

Castillo, L. & George, W. K. 2001 Similarity analysis for turbulent boundary layer with pressure gradient: outer flow. *AIAA* **39**, 41–47.

Clauser, F. H. 1954 Turbulent boundary layers in adverse pressure gradients. *J. Aero. Sci.* **21**, 91–108.

Coles, D. E. & Hirst, E. A. 1969 *Proceeding Computation of Turbulent Boundary Layers – 1968 AFOSR-IFP-Stanford Conference*, vol. 2, pp. 198.

Cutler, A. D. & Johnston, J. P. 1989 The relaxation of a turbulent boundary layer in an adverse pressure gradient. *J. Fluid Mech.* **200**, 367–387.

DeGraaff, D. B. & Eaton, J. K. 1999 Reynolds number scaling of the turbulent boundary layer on a flat plate and on swept and unswept bumps. *Tech. Rep. TSD-118*, Stanford University.

DeGraaff, D. B. & Eaton, J. K. 2000 Reynolds number scaling of the flat plate turbulent boundary layer. *J. Fluid Mech.* **422**, 319–346.

DeGraaff, D. B. & Eaton, J. K. 2001 A high resolution laser Doppler anemometer: design, qualification, and uncertainty. *Exps. Fluids* **20**, 522–530.

Dengel, P. & Fernholz, H. H. 1990 An experimental investigation of an incompressible turbulent boundary layer in the vicinity of separation. *J. Fluid Mech.* **212**, 615–636.

Elsberry, K., Loeffler, J., Zhou, D. & Wygnanski, I. 2000 An experimental study of a boundary layer that is maintained on the verge of separation. *J. Fluid Mech.* **423**, 227–261.

Gillis, J. C. & Johnston, J. P. 1983 Turbulent boundary-layer flow and structure on a convex wall and its redevelopment on a flat wall. *J. Fluid Mech.* **135**, 123–153.

Krogstad, P. & Kaspersen, J. 2002 Structure inclination angle in turbulent adverse pressure gradient boundary layer. *J Fluids Engng* **142**, 1025–1033.

Krogstad, P. A. & Skåre, P. E. 1995 Influence of a strong adverse pressure gradient on the turbulent structure in a boundary layer. *Phys. Fluids* **7**, 2014–2024.

Lu, S. S. & Willmarth, W. W. 1973 Measurements of the structure of the Reynolds stress in a turbulent boundary layer. *J. Fluid Mech.* **60**, 481–511.

Marusic, I. & Kunkel, J. G. 2003 Streamwise turbulence intensity formulation for flat-plate boundary layers. *Phys. Fluids* **15**, 2461–2464.

Mellor, G. L. & Gibson, D. M. 1966 Equilibrium turbulent boundary layers. *J. Fluid Mech.* **24**, 225–253.

Monson, D. J., Mateer, G. G. & Menter, F. R. 1993 Boundary-layer transition and global skin friction measurement with an oil-fringe imaging technique. *SAE Tech. Paper Series 932550.*

Perry, A. E. & Marusic, I. 1995 A wall-wake model for the turbulence structure of boundary layers. Part 1. Extension of the attached eddy hypothesis. *J. Fluid Mech.* **298**, 361–388.

Perry, A. E., Marusic, I. & Jones, M. B. 2002 On the streamwise evolution of turbulent boundary layers in arbitrary pressure gradients. *J. Fluid Mech.* **461**, 61–91.

Perry, A. E. & Schofield, W. H. 1973 Mean velocity and shear stress distributions in turbulent boundary layers. *Phys. Fluids* **16**, 2068–2074.

Samuel, A. E. & Joubert, P. N. 1974 A boundary layer developing in an increasingly adverse pressure gradient. *J. Fluid Mech.* **66**, 481–505.

Skåre, P. E. & Krogstad, P. A. 1994 A turbulent equilibrium boundary layer near separation. *J. Fluid Mech.* **272**, 319–348.

Skote, M. & Henningson, D. S. 2002 Direct numerical simulation of a separated turbulent boundary layer. *J. Fluid Mech.* **471**, 107–136.

Song, S. & Eaton, J. K. 2004 Reynolds number effects on a turbulent boundary layer with separation, reattachment and recovery. *Exps. Fluids* **36**, 246–258.

Spalart, P. R. & Watmuff, J. H. 1993 Experimental and numerical study of a turbulent boundary layer with pressure gradients. *J. Fluid Mech.* **249**, 337–371.

Tsuji, Y. & Morikawa, Y. 1976 Turbulent boundary layer with pressure gradient alternating in sign. *Aero. Q.* **27**, 15–28.

Tulapurkara, E. G., Khoshnevis, A. B. & Narasimhan, J. L. 2001 Wake–boundary layer interaction subject to convex and concave curvatures and adverse pressure gradient. *Exps. Fluids* **31**, 697–707.

Wallace, J. M., Eckelmann, H. & Brodkey, R. S. 1972 The wall region in turbulent shear flow. *J. Fluid Mech.* **54**, 39–48.

Zagarola, M. V. & Smits, A. J. 1998 Mean-flow scaling of turbulent pipe flow. *J. Fluid Mech.* **373**, 33–79.